

GT2020-16277

DESIGN SPACE EXPLORATION OF STAGNATION TEMPERATURE PROBES VIA DIMENSION REDUCTION

Ashley D. Scillitoe^{†*}, Bryn Ubald[†], Pranay Seshadri^{†+×}, Shahrokh Shahpar[‡]

[†]The Alan Turing Institute, London, U.K.

[‡]University of Cambridge, Cambridge, U.K.

[‡]Rolls-Royce plc., Derby, U.K.

[×]Imperial College London, London, U.K.

ABSTRACT

The measurement of stagnation temperature is important for turbomachinery applications as it is used in the calculation of component efficiency and engine specific fuel consumption. This paper examines the use of polynomial variable projection to identify dimension reducing subspaces for stagnation temperature probes. As an example application we focus on a simplified Kiel probe geometry, but the proposed data-centric approach could be readily applied to new datasets with different geometries, boundary conditions and design objectives.

The design of Kiel probes is non-trivial, with a large design space, complex flow physics, and competing design objectives. Two design objectives are considered: (1) the stagnation pressure loss, to reduce instrumentation losses; (2) the change in recovery ratio with respect to Mach number, to reduce temperature measurement uncertainty.

Subspaces are obtained for the two design objectives, allowing the influence of seven design parameters to be understood. The entropy generation rate is used to provide physical insights into loss mechanisms. The recovery ratio subspace indicates that for the present probe there is an optimum vent-to-inlet area which minimises the change in recovery ratio with respect to Mach number, and design modifications that yield further small improvements are explored.

Finally, the uncertainty in recovery ratio due to manufacturing variability is shown to be important. In comparison to global sensitivity measures, the use of an active subspace is shown to provide important information on what manufacturing tolerances are important for specific designs. New designs can also be selected that are insensitive to given manufacturing tolerances.

1 INTRODUCTION

Accurate and precise temperature measurements are vital for advances in aerothermal technology. In engine tests, these values are the output of elaborate measurement chains that originate at temperature probes installed at various locations in an engine (see Fig. 1). Millivolt scale perturbations are induced at the hot junction of each probe, following which these signals traverse through a series of filters, amplifiers, multiplexers and an analog-to-digital converter before being finally converted into Kelvin on a computer (see page 79 in [1]). Throughout this chain, uncertainties are aggregated owing to temporal averaging, spatial averaging, static calibration, cold junction temperature measurement and the design of the temperature probe itself. The latter can give rise to convection, conduction, radiation and velocity errors, warranting further study into the probe and its aerothermal environment.

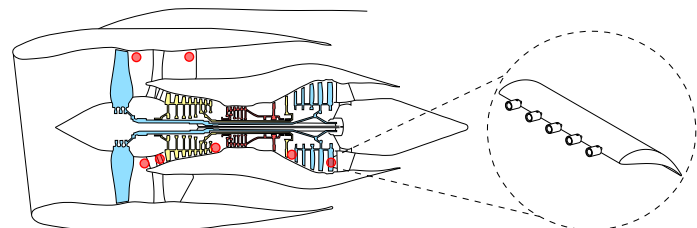


FIGURE 1: Temperature measurement locations (circled in red) for a typical 3-shaft turbofan engine and an archetypal turbine probe arrangement. Based upon Ref. [2].

Prior to burrowing down this path, it will be useful to understand

*Address all correspondence to ascillitoe@turing.ac.uk

the wider impact of imprecise measurements in an engine. Bonham et al. [3] state that for accurate turbomachinery efficiency measurements to within $\pm 1\%$, one requires uncertainties in stagnation temperature to be within $\pm 0.1\%$ —a reflection of the challenging aerothermal outlook. In their study on temperature measurements for a turbine, Seshadri et al. [4] estimate that with aero-engine industry representative uncertainties of $\pm 2.4K$ at 68% percentile for stagnation temperature, a $\pm 1.2\%$ uncertainty in efficiency can be expected.

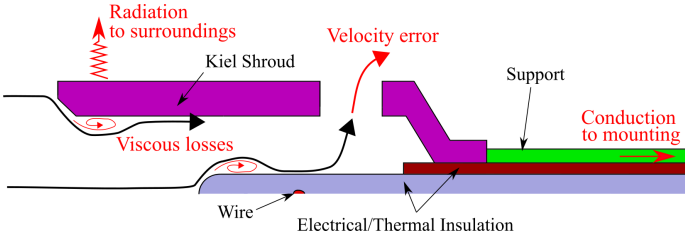


FIGURE 2: The main sources of radiative, velocity and conductive errors in a Kiel shrouded stagnation temperature probe.

A typical Kiel probe configuration used for temperature measurements is shown in Figure 2. Thermocouple wires are encased within a Kiel shroud [5], which acts to bring the flow to near stagnation conditions, as well as to desensitise the measurements to inflow angle. However, the low velocity over the thermocouple wires reduce the convective heat transfer to them, causing the probe to become sensitive to conductive (and radiative) heat transfer to the surroundings. This *conductive error* can be abated by increasing the flow through the bleed holes, but a *velocity error* then arises since the velocity over the thermocouple is further from stagnation conditions (see Ref. [1] for further details). Flow separation and other viscous flow effects also lead to a loss of stagnation temperature.

Due to their size relative to surrounding blades, probes can also have a significant influence on the flow they are trying to measure. Luo [6] finds that leading edge probes have an important effect on the loading of compressor blades. Meanwhile, Ng and Coull [7] show that probes influence the boundary layer transition, as well as the profile losses, across turbine blades.

Concurrently, with the continued drive for performance gains in gas turbine engines, there is a clear need for more accurate and less intrusive temperature probes. A number of modifications to the standard Kiel probe have been proposed, such as dual shrouded probes [3]. Ng and Coull [7] have explored how basic design features of a standard Kiel probe, such as probe diameter and length, can influence the probe's performance.

More broadly, these efforts echo the objective of numerous aerothermal design studies, where one is interested in understanding which key parameters have a strong influence on reducing pressure loss, increasing efficiency, or decreasing *SFC*, and why. Such a *sensitivity analysis* seeks to rank all the design parameters based on their importance, and interaction with other parameters, via metrics ranging from local sensitivity indices such as gradients to more

global indices such as elementary effects [8], Sobol' indices and the related derivative- [9] and total-effects-based [10] variance measures. Through the ranking obtained, one can confirm which *subset of parameters* are the primary drivers of aerothermal performance and thus discard the remainder from further parametric studies. Unfortunately, computing such metrics in the first place requires the execution of a suitable design of experiment, which can be computationally prohibitive with more design parameters. To tackle the *curse of dimensionality* associated with such design of experiments, we deviate from such *subset-based* strategies and adopt a *subspace-based* stratagem of dimension reduction based on *ridge approximations* [11].

Ridge approximations and the closely related *active subspaces* [12] constitute a class of computational heuristics and data-driven algorithms for querying which *linear combination of parameters* are important. They have seen use in a range of turbomachinery-based design and aerothermal analysis studies, ranging from preliminary mean-line design [13]; multi-point fan blade design [14]; design space maps [15] and manufacturing assessments [16]. In this paper, we leverage the insight afforded by ridge approximations to better understand the design space of a Kiel shrouded probe. The approach taken here is *data-centric*, in that it is applied a posteriori to a CFD dataset. The same approach could be readily applied to new datasets with different geometries, boundary conditions and design objectives.

The remainder of this paper is structured as follows: in Sec. 2 the design objectives considered in the paper are outlined. After a presentation of the underlying methods used in Sec. 3, in Sec. 4 dimension reducing subspaces are computed and explored. An example of how these subspaces assist in finding new probe designs is then given in Sec. 5. Finally, in Sec. 6, the idea of using dimension reducing subspaces to find designs that are insensitive to manufacturing uncertainties is explored.

2 DESIGN OBJECTIVES

A number of design objectives are to be considered in this paper. Firstly, Ubald et al. [2] found that over 50% of the stagnation pressure losses observed at the exit to a linear turbine cascade were due to the presence of leading edge temperature probes. It is important to reduce this, hence the first quantity considered is the *pressure loss coefficient*

$$Y_p = 100 \frac{P_{0,in} - P_{0,out}}{P_{0,in} - P_{out}} (\%), \quad (1)$$

where $P_{0,out}$ and P_{out} are the stagnation and static pressure mass-averaged across the outlet of the computational domain, and $P_{0,in}$ is the inlet stagnation pressure. Since probes are subjected to a range of Mach numbers in an engine, the average Y_p across the set of Mach numbers $\mathbf{M} = \{0.3, 0.4, 0.5, 0.6, 0.7, 0.8\}$ is taken to give the loss design objective, which we wish to minimise,

$$O_{Y_p} = \frac{1}{6} \sum_{M \in \mathbf{M}} Y_p(M). \quad (2)$$

The second performance parameter to consider is the probe's *recovery ratio*. Due to the conduction and velocity errors mentioned in Section 1, the temperature measured by the probe, T_m , is not equal to the real stagnation temperature T_0 . The probe's temperature recovery properties must be known in order for the true temperature T_0 to be obtained. This can be in the form of the probe's recovery ratio $R_r = T_m/T_0$, or its recovery factor $R_f = (T_m - T)/(T_0 - T)$ [17], where T is the freestream static temperature. Many practitioners (e.g. [7]) use R_f , since it better accounts for the changing dynamic head of the flow. However, as noted by Smout [18]: "where the dynamic head is small, the error in experimentally determined recovery factor can easily be greater than the error that would occur if no recovery correction were made to measured data". For this reason, and for simplicity, many studies (e.g. [19, 20]) use R_r , as is done in this paper. It would, however, be straightforward to apply the same approach with R_f .

The Mach number of the surrounding flow alters the convective heat transfer coefficient to the thermocouple, as well as the temperature gradient driving conduction. Therefore, the recovery ratio is a function of Mach number, and R_r (or R_f) versus Mach number curves like those in Figure 3a must be obtained during probe calibration. When these curves are used for post-test recovery error corrections, any uncertainty in Mach number will lead to an uncertainty in R_r , and therefore in T_0 . To minimise this uncertainty, the second design objective to be minimised is taken as the gradient of recovery ratio with respect to Mach number.

$$O_{R_r} = \left| \frac{\partial R_r(M)}{\partial M} \right| \quad (3)$$

As the R_r curves for the probes explored in this paper were close to linear (see Fig. 3a), the gradient was obtained by performing ordinary least squares linear regression on R_r across the set \mathbf{M} .

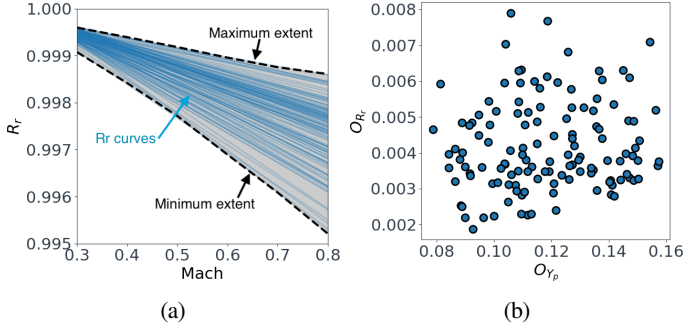


FIGURE 3: (a) Recovery ratio versus Mach number curves and (b) design objectives for all 128 probe designs explored in this paper.

As seen in Figure 3b, the worst probes explored in this paper have values of up to $O_{R_r} = 0.0079$. For a Mach number uncertainty of $M \pm 0.02$, this would lead to uncertainty in R_r of $\pm 0.02 \times 0.0079 = \pm 1.6 \times 10^{-4}$, and a temperature uncertainty of $T_0 \pm 0.016\%$. Although small, this uncertainty is not insignificant

if aiming for the $T_0 \pm 0.1\%$ uncertainty target given by Bonham et al. [3]. Bonham et al. [19] reports a smaller measurement uncertainty of $M \pm 0.006$, however $M \pm 0.02$ may be realistic if the pitot-static probe used to measure M is located some distance from the temperature probe, or if M is estimated by other means.

Bonham et al. [19] examines the temperature measurement error due to flow unsteadiness. This arises when recovery ratio curves obtained in a steady aerodynamic calibration facility are used to correct measured temperatures in an unsteady flow. The probe with the smallest unsteady error was found to be the one with the smallest R_r versus Mach gradient. Since many turbomachinery flows are unsteady, this further incentivises minimisation of the O_{R_r} objective.

Complex probe designs, such as the dual shrouded probe design of Bonham et al. [3], have been proposed to minimise Mach number sensitivity [3]. This paper will examine whether the same can be achieved through judicious exploration of the design space for a more simple single shrouded probe. As Figure 3b shows, the two design objectives O_{Y_p} and O_{R_r} are not strongly correlated. A multi-objective optimisation could be performed to find designs which minimise both design objectives at once. However, as this paper will demonstrate, in addition to finding better designs, dimension reducing subspaces can provide a more comprehensive understanding of the design space.

3 METHODS

The baseline geometry, and the seven design parameters which parametrise it, are shown in Figure 4. The geometry studied here is a real temperature probe used in engine tests, and has been investigated in detail in Ref. [2]. The thermocouple is sheathed with Inconel 600, and the thermocouple wires are insulated with a layer of MgO. The wires and the insulation are both modelled, with the material properties of both the NiSil and NiCroSil wires being averaged to enable the use of a symmetry plane to reduce computational costs. The upper and lower extents of the design space are given by the vectors \mathbf{x}^L and \mathbf{x}^U in Table 1.

TABLE 1: Lower \mathbf{x}^L and upper \mathbf{x}^U extents of the design space. Parameters are given as delta's from the baseline design, \mathbf{x}^0 , since the absolute dimensions are proprietary.

Design parameter	\mathbf{x}^L	\mathbf{x}^0	\mathbf{x}^U
1. Ellipsoidal hole (scale)	0.50	1.00	1.25
2. Move hole (translate)	-0.3mm	0.0mm	0.0mm
3. Angle hole (translate inner)	0mm	0.0mm	1.0mm
4. Kiel leading edge (translate)	-2.0mm	0.0mm	2.0mm
5. Kiel outer diameter (scale)	0.90	1.00	1.25
6. Kiel inner diameter (scale)	0.75	1.00	1.10
7. Bleed hole diameter (scale)	0.50	1.00	1.50

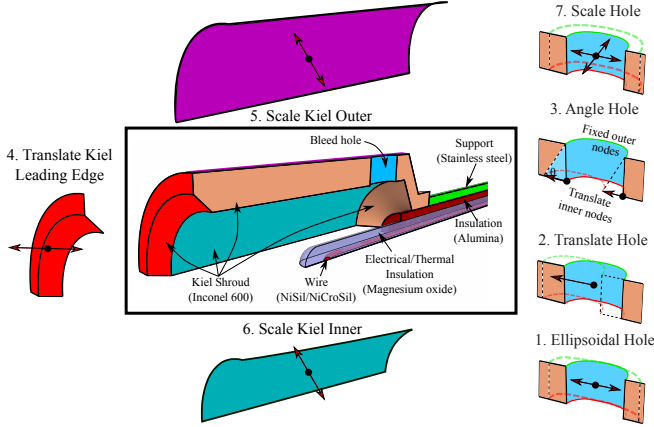


FIGURE 4: Cross-section of the probe design explored in this paper. Material types are labelled within the inner box. The 7 design parameters modified are shown in the outer region.

To sample the design space, N number of designs are drawn uniformly between $[\mathbf{x}^L, \mathbf{x}^U]$ to obtain unique $\hat{\mathbf{x}}_j$ design vectors ($j=1,\dots,N$), each with $d=7$ elements (or rows) corresponding to the number of design variables. There are numerous heuristics for drawing these *design of experiment* (DOE) samples (see [14] for details); in this paper, optimal Latin hypercube sampling (LHS) with $N=128$ chosen¹. The selection of $N=128$ should be sufficient, since from prior experience, N should be at least 4 to 5 times d (this is verified by checking R^2 scores for different N , similar to Sec. 4). A full factorial DOE, with 3 levels for each design parameter, would require 2,187 design samples, therefore the use of LHS offers a significant cost saving.

Next, for each sample

$$\mathbf{x}_j = \frac{2\hat{\mathbf{x}}_j - (\mathbf{x}^U - \mathbf{x}^L)}{(\mathbf{x}^U - \mathbf{x}^L)} \quad (4)$$

was computed. Equation 4 transforms all the dimensionalised samples to lie between $\mathbf{x}_j \in [-1, 1]^7$. For each \mathbf{x}_j , a geometry can be discretised using the mesh morphing procedure in Section 3.1. Each case is then run through a computational fluid dynamics (CFD) solver, described in Section 3.2, and the design objectives O_{Y_p} and O_{R_r} evaluated for each design.

3.1 Mesh morphing

Generating 128 CFD meshes from scratch would be prohibitively time consuming. Instead, a baseline mesh is created, and the 128 meshes are generated by morphing the baseline mesh. A parallelised mesh morphing tool has been created [21] in C++ using a Radial Basis Function (RBF) based morphing method similar to that used by de Boer et al. [22]. For this method, an interpolation

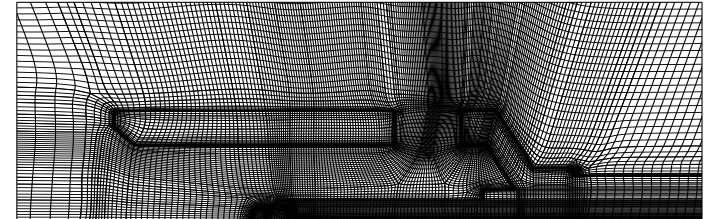
¹This can be replaced with Monte Carlo or other sampling heuristics with no significant change in the results, provided that the sampling density is uniform.

function is used to define the nodal displacement based on the weighted sum of a basis function ϕ :

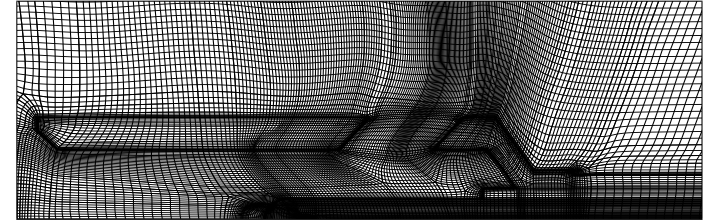
$$s(z) = \sum_{i=1}^M w_i \phi(||z - z_{k_i}||) \quad (5)$$

where z_{k_i} is a vector of control points with pre-defined displacements, M is the number of control points, and w_i is a vector of the interpolation weights. A number of options were considered for the RBF kernel function, ϕ . The Wendland C^0 function was selected due to its compact support resulting in a sparse coefficient matrix and significantly lower runtime.

Due to the sharp rise in the cost of the RBF method with increasing evaluation points, the deformation of the 7 design parameters was completed independently and successively to each other, hence, each of the 128 meshes required the generation of 7 prior meshes. All of the meshes were generated on the Cambridge CSD3 cluster with 320 cores (Each node has dual Intel® Xeon® Gold 6142 for a total of 32 cores per node and 384GB of RAM), taking a total of approximately 4,000 CPU hours.



(a) Baseline structured mesh



(b) A morphed mesh

FIGURE 5: Example of meshes generated for this study.

A quarter of the baseline probe is meshed, with symmetry planes in the y and z directions. A baseline structured multi-block mesh was generated, with ~ 4 million nodes required to achieve satisfactory mesh independence. The baseline mesh is shown in Figure 5a. The solid regions are also meshed, with fully conformal interfaces between all fluid/solid regions. Mesh refinement is performed at the interfaces to ensure $y^+ < 1$ in the fluid domain. An example deformed mesh is shown in Figure 5b.

3.2 CFD predictions

To obtain flow fields for each probe geometry we solve the 3D, compressible, Reynolds-averaged Navier-Stokes (RANS) equations on the aforementioned meshes using the ANSYS Fluent CFD solver. The CFD simulations are fully coupled conjugate simulations, with conductive heat transfer modelled in the solid regions. The wires and their insulating material are discretised, but it is not feasible to model the wires all the way to the reference junction. Instead, the stem and its encompassing solid regions are extended $\approx 11D$ (where D is the probe diameter) downstream, in a similar manner to the approach of Schneider [23] and Quickel [24]. The different materials that are modelled in this study are labelled in Figure 4.

Simulations are run at 6 different Mach numbers (see Tab. 2), leading to 768 CFD simulations in total. For each Mach number the inlet stagnation temperature $T_{0,in}$ is adjusted so that the inlet static temperature remains constant at 300k. The outlet static pressure was fixed at $P_{out} = 101,325$ Pa, with the inlet/outlet located $5D$ and $25D$ upstream/downstream from the probe leading/trailing edges. The probe is modelled as a *probe in freestream*, with the temperature of the support, insulation and wires unconstrained at the domain outlet. A significant amount of heat is still conducted away from the probe since the flow downstream of the probe convects heat away from the lengthened support. However, this simplification, and the lack of radiative heat transfer in the simulations, mean that the velocity error is expected to play a more dominant role compared to the real probe.

TABLE 2: Inlet boundary conditions.

M	$P_{0,in}$ (Pa)	$T_{0,in}$ (K)
0.3	107,850	305
0.4	113,136	310
0.5	120,196	315
0.6	129,241	322
0.7	140,553	329
0.8	154,459	338

Previous work by one of the authors [25] studied the performance of a number of RANS models for the simulation of a dual shrouded probe in freestream. The Realizable $k - \varepsilon$ model with streamline curvature and Kato-Launder stagnation corrections was found to perform best, and this setup is chosen for the present study. The inflow k and ε are set to give an inflow turbulence intensity of 0.5% and a viscosity ratio of 5. All simulations were completed on the Cambridge CSD3 cluster. Each case was run using 16-24 dual Intel® Xeon® Gold 6142 compute cores (depending on license availability) for a total compute time of approximately 20,000 CPU hours.

3.3 Ridge approximation and dimension reduction

As before, let $\mathbf{x} \in \mathbb{R}^d$ (with $d = 7$) represent a *sample* within our design space χ and within this space let $f(\mathbf{x})$ represent our aerothermal functional, which could be either $O_{Y_p}(\mathbf{x})$ or $O_{R_r}(\mathbf{x})$. Our goal is to construct the approximation

$$f(\mathbf{x}) \approx g(\mathbf{U}^T \mathbf{x}), \quad (6)$$

where $\mathbf{U} \in \mathbb{R}^{d \times m}$ is an orthogonal matrix with $m \ll d$, implying that g is a polynomial function of m variables—ideally $m = 1$ or $m = 2$ to facilitate easy visualization. In addition to m , the polynomial order of g , given by k , must also be chosen. The matrix \mathbf{U} isolates m linear combinations of *all* the design parameters that are deemed sufficient for approximating f with g . Techniques for determining the unknowns \mathbf{U} and g in literature [26, 27] are rooted around solutions to the non-linear least squares problem

$$\underset{\mathbf{U}, \boldsymbol{\alpha}}{\text{minimize}} \|f(\mathbf{x}) - g_{\boldsymbol{\alpha}}(\mathbf{U}^T \mathbf{x})\|_2^2, \quad (7)$$

where $\boldsymbol{\alpha}$ represents unknown model variables associated with g . In practice, to solve this optimization problem, we assemble the N input-output data pairs

$$\mathbf{X} = \begin{bmatrix} \mathbf{x}_1^T \\ \vdots \\ \mathbf{x}_N^T \end{bmatrix}, \quad \mathbf{f} = \begin{bmatrix} f_1 \\ \vdots \\ f_N \end{bmatrix}, \quad (8)$$

and replace $f(\mathbf{x})$ in (7) with the evaluations \mathbf{f} . Algorithms for solving this problem include [26], where the authors propose an alternating optimization problem where g is the posterior mean of a Gaussian process and $\boldsymbol{\alpha}$ are the hyperparameters associated with a pre-defined kernel function. Here, we adopt the *polynomial variable projection approach* of Hokanson and Constantine [27] where g is a polynomial and $\boldsymbol{\alpha}$ are its coefficients. Both \mathbf{U} and $\boldsymbol{\alpha}$ are obtained by recasting (7) as a separable non-linear least squares problem using the idea of variable projection (see Golub and Pereyra [28]), resulting in a solution via a Gauss-Newton optimization. This code can be found in the open-source Effective-Quadratures² python package [29]. The non-dimensionalised data for the probe studies and the underlying scripts can be found at github.com/ascillitoe/probe-subspaces.

4 OBTAINING DIMENSION REDUCING SUBSPACES

From the N number of CFD evaluations we obtain values for the design objectives $O_{Y_p}^j$ and $O_{R_r}^j$ for each design \mathbf{x}_j . The design vectors \mathbf{x}_j lie in a 7 dimensional hypercube

$$\chi \subset [-1, 1]^7 \quad \text{where} \quad \mathbf{x}_j \in \chi \quad \text{for} \quad j = 1, \dots, N, \quad (9)$$

²www.effective-quadratures.org

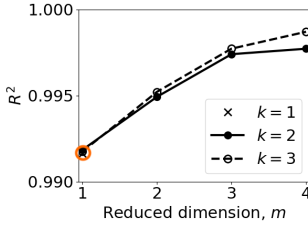
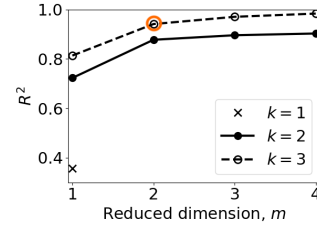
(a) Loss objective, O_{Y_p} (b) Recovery objective, O_{R_r}

FIGURE 6: R^2 scores versus reduced dimensions m and polynomial order k , with selected combinations highlighted in orange.

which makes exploration of the design space difficult. To reduce the dimensionality of the problem, we wish to use the method of variable projection (Sec. 3.3) to obtain dimension reducing subspaces for the two design objectives. To elaborate on Equation 6, we wish to approximate each design objective with a reduced dimension polynomial,

$$O_{Y_p}(\mathbf{x}_j) \approx g(\mathbf{U}_Y^T \mathbf{x}_j) \quad (10)$$

$$O_{R_r}(\mathbf{x}_j) \approx h(\mathbf{U}_R^T \mathbf{x}_j), \quad (11)$$

where $\mathbf{U}_Y^T \in \mathbb{R}^7$ and $\mathbf{U}_R^T \in \mathbb{R}^{7 \times 2}$. But first, suitable values for the polynomial order k and reduced dimension m must be found. For ease of interpretation and visualisation it is desirable to work with small values of m , while small values of k (i.e. $k \leq 3$) prevent over-fitting. Variable projection is applied with different values of k and m , and R^2 scores are obtained by comparing the *polynomial approximation* $g(\mathbf{U}^T \mathbf{x}_j)$ to the *true CFD results* O_{Y_p} .

Figure 6 shows the R^2 scores for all combinations of k and m tested. For O_{Y_p} , increasing m gives a slightly higher R^2 score, but $R^2 = 0.992$ with $m=1$ and $k=1$ is already satisfactory. For O_{R_r} , slightly higher R^2 scores are obtained with $m > 2$. However, this would be at the expense of interpretability, therefore in this instance we stick with a 2 dimensional ($m=2$) subspace. Increasing the polynomial order to $k=3$ yields an appreciable increase in the R^2 score in this case. The final choice of $m=2$ and $k=3$ gives an R^2 score of 0.941 for O_{R_r} .

4.1 The pressure loss subspace

The high R^2 score of the dimension reducing subspace for the loss design objective indicates that O_{Y_p} admits low dimensional structure. In other words, minimal information has been lost by reducing the dimension, and we can construct a *sufficient summary plot* to summarise the behaviour of O_{Y_p} in our reduced dimensional space. In Figure 7, the true O_{Y_p} values are plotted against the inputs, \mathbf{x}_j , projected onto the loss subspace i.e. $u_Y = \mathbf{U}_Y^T \mathbf{x}$. It is clear that the actual CFD evaluations (circular markers) lie close to the polynomial approximation $g(\mathbf{U}_Y^T \mathbf{x}_j)$, which we have chosen to be linear ($k=1$) in this case.

The orange circle in Figure 7 highlights the baseline design. It is apparent that designs with lower loss exist for lower u_Y . Examining

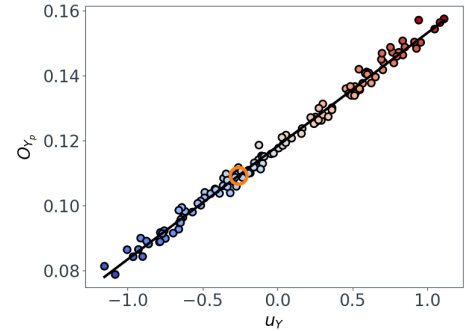


FIGURE 7: Sufficient summary plot for the loss design objective O_{Y_p} , plotted on its active subspace.

\mathbf{U}_Y in Equation 12, which projects the 7 dimensional \mathbf{x} onto the 1 dimensional subspace, tells us how the designs change as the 1 dimensional space is traversed.

$$\mathbf{U}_Y = [0.05, 0.01, \underbrace{-0.12}_{\text{Angle hole}}, -0.02, \underbrace{0.98}_{\text{Kiel } \otimes_{\text{outer}}}, 0.02, \underbrace{0.17}_{\text{Hole } \otimes}] \quad (12)$$

The 7 elements in \mathbf{U}_Y are the weights corresponding to the 7 design variables in Table 1. The weight for Kiel outer diameter is close to 1, indicating that the parameter changes almost from its minimum to maximum value as u_Y goes from -1 to 1. Figure 7 tells us that O_{Y_p} increases linearly as this is done. The next two largest weights in \mathbf{U}_Y are the bleed hole angle and diameter. The hole angle parameter is seen to decrease slightly as u_Y is increased, while the hole diameter increases. This suggests that higher angled bleed holes³ decrease loss, while larger hole diameters increase it. To further elucidate these findings, the sources of loss are examined by thinking of loss in terms of an increase in entropy [30]. The total entropy generation rate per unit volume is the sum of the entropy generation due to heat transfer \dot{S}_{ht} , and the entropy generation due to viscous effects \dot{S}_v . The heat transfer term is an order of magnitude smaller than the viscous term in this case, so we focus on the viscous term

$$\dot{S}_v = \frac{1}{T} (\tau_{ij} : \nabla u), \quad (13)$$

where τ_{ij} is the combined viscous and turbulent stress tensor, and T is the static temperature. The viscous term is calculated from CFD results for two designs at either end of the O_{Y_p} subspace, and contours are presented in Figure 8.

The high loss design exhibits large amounts of viscous entropy generation in three key regions, labelled in Figure 8a:

³As shown in Figure 4, the hole angle parameter is defined as a translation of the inner bleed hole opening to the fore, so decreasing this parameter leads to less angled holes.

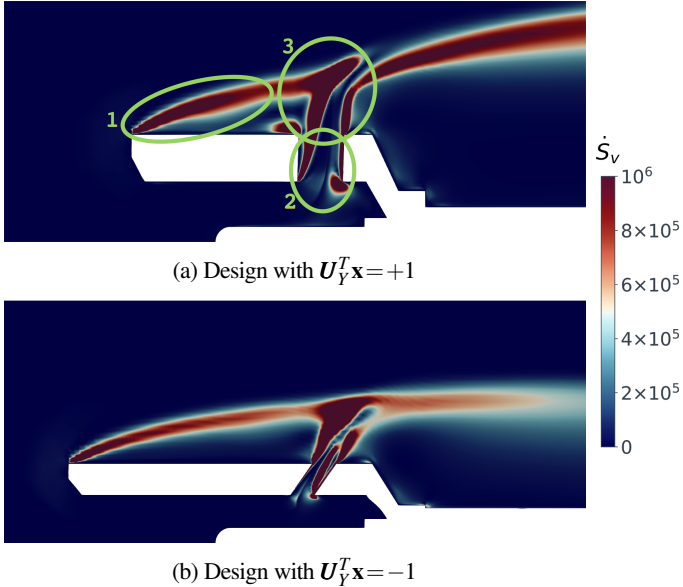


FIGURE 8: Contours of viscous entropy generation rate, from CFD for $M=0.8$, for designs at either end of the loss subspace.

- Leading edge shear layer** - The flow separates at the leading edge of the shroud, and a separated shear layer convects downstream. As expected [30], the viscous friction in the free shear layer generates significant entropy.
- Bleed hole interior**: A stagnation point on one of the inner bleed hole corners, and a separated shear layer emanating from the other, generate noticeable amounts of entropy.
- Bleed hole exit** - The flow ejected from the bleed holes is representative of a jet in crossflow. Studies have shown that such jets interact with the mean flow and generate kidney-vortices [31]. Recent large eddy simulations [2] of a temperature probe have highlighted the parasitic loss caused by these vortices.

In comparison, the low loss design in Figure 8b has lower entropy generation rates in these three key areas. Ng and Coull [7] suggest that a similar probe behaves like a bluff body, with decreasing probe diameter leading to a smaller frontal area and less bluff body drag. The present comparison appears to agree here, with the reduced outer diameter of the low loss design (Fig. 8b) leading to a weaker shear layer originating from the leading edge. Adding a bleed hole angle has reduced the severity of the stagnation and separation regions within the bleed hole interior, leading to lower entropy generation here. Additionally, the sweptback hole reduces the angle between the exiting jet and the freestream, leading to less pronounced jet in crossflow effects and less entropy generation here.

4.2 The recovery ratio gradient subspace

Exploring the subspace for the recovery ratio design objective is more involved, since we have chosen a cubic polynomial with 2

reduced dimensions in this case. Figure 9 is the sufficient summary plot for this design objective. The two horizontal axes are the physical coordinates \mathbf{x} , projected onto the two reduced subspace dimensions $u_{R,1}$ and $u_{R,2}$, where

$$\begin{aligned}\mathbf{u}_R &= \mathbf{U}_R^T \mathbf{x} \\ &= [u_{R,1} \quad u_{R,2}].\end{aligned}\quad (14)$$

Generally, the markers denoting the true O_{R_r} values collapse closely onto the coloured surface in Figure 9, which is the polynomial approximation for O_{R_r} . The objective O_{R_r} displays a mostly quadratic behaviour in the $u_{R,1}$ direction, with designs that have significantly lower recovery ratio sensitivity to Mach number (low O_{R_r}) existing around $u_{R,1}=0.4$.

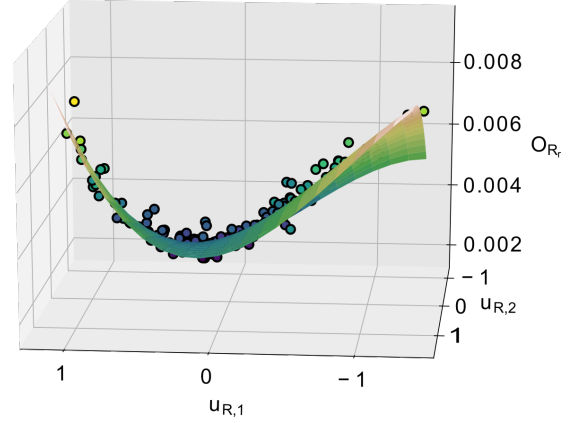


FIGURE 9: Sufficient summary plot for the recovery ratio design objective O_{R_r} , plotted on its active subspace.

The O_{R_r} subspace is viewed in a top-down fashion in Figure 10a. As already observed, O_{R_r} displays quadratic behaviour in the direction of the vector $\mathbf{v}_a = (1.0, 0.0)$. A physical interpretation of how designs vary along this vector is given by the elements of the vector product $\mathbf{v}_a \mathbf{u}_R$, shown in Figure 11a. The elements can be directly compared since we have non-dimensionalised the input data such that $\mathbf{x}_j \in [-1, 1]^7$. It is primarily the bleed hole diameter and hole ellipse which increase as we move along the vector \mathbf{v}_a , with the Kiel inner diameter decreasing slightly.

The bleed hole diameter and Kiel inner diameter are important since they control the probe's vent area and inlet area. The ratio of vent-to-inlet area (A_{vent}/A_{inlet}) controls the Mach number over the thermocouple junction [17]:

$$M_j = M_\infty \frac{A_{vent}}{A_{inlet}} \left(1 + \frac{\gamma-1}{2} M_\infty^2 \right)^{\frac{-1}{\gamma-1}}. \quad (15)$$

Markowski and Moffatt [17] advise that in order to maximise recovery ratio, M_j must be sufficiently small ($M_j \leq 0.25$) to minimise velocity

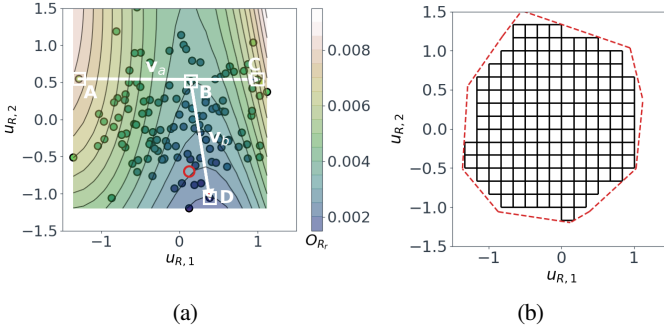


FIGURE 10: The recovery ratio subspace with: (a) contours of the polynomial approximation of O_{R_r} and markers showing the discrete design points; (b) a Cartesian grid drawn across the convex hull of the projection of the design points in the subspace.

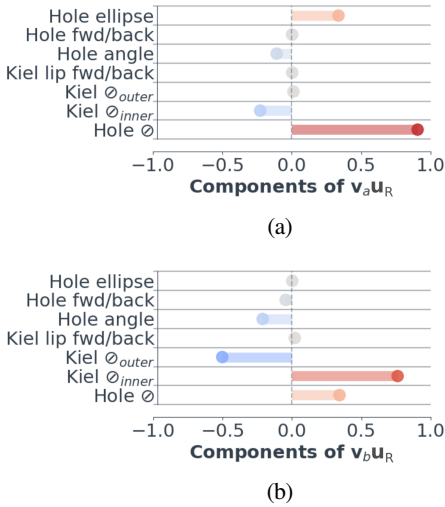


FIGURE 11: Weights of the vectors (a) $\mathbf{v}_a \mathbf{u}_R$ and (b) $\mathbf{v}_b \mathbf{u}_R$.

errors (see Sec. 1). However, if it is too small the convective heat transfer will be too low and *conductive errors* will become more significant. Equation 15 is rearranged to give the area ratio required for a given M_j , and is plotted in Figure 12a. It is apparent that the area ratio required for a given M_j strongly depends on M_∞ , and thus the optimal area ratio required to maximise recovery also depends on M_∞ .

Along the vector \mathbf{v}_a the bleed hole diameter increases while the Kiel inner diameter decreases, meaning the ratio A_{vent}/A_{inlet} is increasing. As O_{R_r} displays quadratic behaviour along the vector, there must also be an optimum value of A_{vent}/A_{inlet} which minimises O_{R_r} , the gradient of R_r with respect to Mach number. Recovery ratio curves for the designs A, B and C that lie on \mathbf{v}_a in Figure 10 are shown in Figure 12b. All three designs have similar values of R_r at Mach 0.3, but R_r falls off quicker with Mach number for designs A and C.

Mach number contours (for $M_\infty=0.8$) and A_{vent}/A_{inlet} ratios for

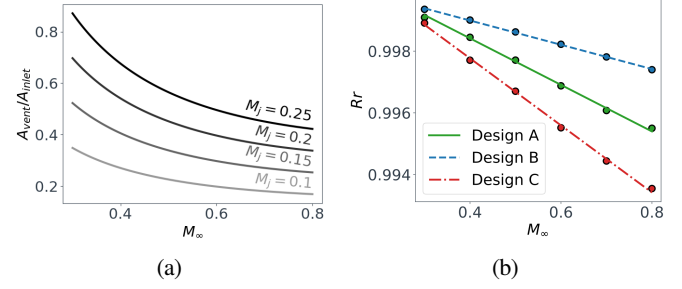


FIGURE 12: Effect of freestream Mach number on: (a) Vent-to-inlet area required to obtain a Mach number M_j over the thermocouple; (b) Recovery ratio for designs A, B and C labelled in Figure 10.

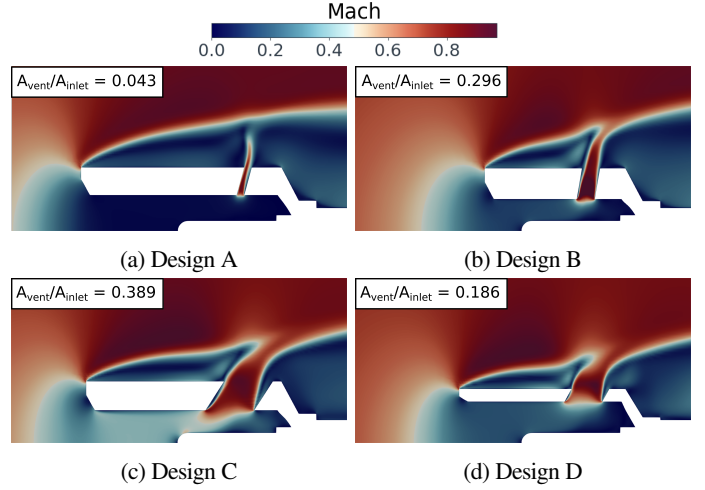


FIGURE 13: Mach number contours for designs A, B, C and D labelled in Figure 10, from CFD for $M=0.8$.

the three designs are shown in Figure 13. The low recovery ratio's at $M_\infty=0.8$ for designs A (Fig. 13a) and C (Fig. 13c) are explained by the overly low and high Mach numbers over the thermocouple. Figure 12a suggests that for $A_{vent}/A_{inlet}=0.389$ (design (c)) a value of $M_j \approx 0.23$ is expected at $M_\infty = 0.8$. However, close to the thermocouple the Mach number is clearly higher than this (Fig. 13c), due to the thermocouple's proximity to the bleed hole and the hole angle. Design (b) (Fig. 13b), which is close to the minimum O_{R_r} value along vector \mathbf{v}_a in Figure 10a, has an area ratio of $A_{vent}/A_{inlet}=0.296$. This is close to the value used by others, such as the PRT probe tested by Bonham et al. [20] which has $A_{vent}/A_{inlet}=0.27$.

Additionally, a slight decrease in O_{R_r} can be obtained by moving in the direction of the vector $\mathbf{v}_b = (0.15, -0.99)$. The elements of $\mathbf{v}_b \mathbf{u}_R$ are visualised in Figure 11b. Moving along this vector primarily involves an increase in the Kiel inner diameter, while simultaneously decreasing the Kiel outer diameter. The effect of this is to reduce the thickness of the shroud, as observed by comparing design D (Fig. 13d) to design C (Fig. 13c).

Clearly, the area ratio A_{vent}/A_{inlet} is significant in determining the recovery ratio, and the recovery ratio's sensitivity to Mach number. However, other design parameters, such as the bleed hole angle and Kiel outer diameter have also been demonstrated to be important. The “optimal” value of A_{vent}/A_{inlet} seen here should not be taken as a design recommendation, since as discussed in Section 3.2, the velocity errors may be overly dominant in the simplified example considered in this paper.

4.3 Considering multiple objectives

So far the two design objectives have been considered in isolation. To properly understand the design space, it is important to consider the two objectives together. This can be done by projecting values of O_{Y_p} onto the O_{R_r} subspace. To begin, a Cartesian grid is drawn within the convex hull (or *perimeter*) of design points that populate the O_{R_r} subspace⁴, as shown in Figure 10b. We wish to find the loss at each point within this grid, using the polynomial approximation for O_{Y_p} . However, there are infinitely many 7 dimensional coordinates \mathbf{x}_j that can be projected onto a given coordinate $u_{R,j}$ in the dimension reducing subspace. We use the hit and run algorithm from [32], also available in *Effective Quadratures* [33], to generate a large number ($N_D = 1000$) of designs at each point in the Cartesian grid.

The N_D designs at each $u_{R,j}$ are expected to have approximately equal values of O_{R_r} , but there is no guarantee they will have similar values of O_{Y_p} . Figure 14a shows that the standard deviation of the O_{Y_p} values can be up to 18% of the mean O_{Y_p} towards the centre of the O_{R_r} subspace. As we are interested in designs with low loss, we take the minimum O_{Y_p} value to plot at each point in Figure 14b.

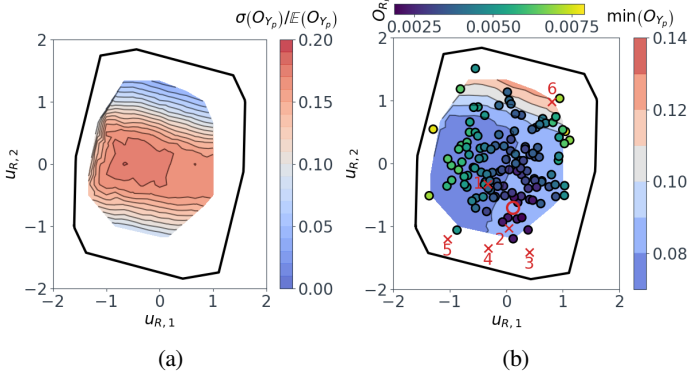


FIGURE 14: The (a) variance and (b) minimum of the loss objective projected onto the recovery ratio objective’s subspace.

The red circle in Figure 14b denotes the baseline design. The O_{R_r} subspace confirms that the baseline design is already relatively good, since it is in the valley of O_{R_r} (refer to the coloured markers for O_{R_r} values). However, slightly lower values of O_{R_r} can be achieved by moving roughly in the direction of \mathbf{v}_b (recall Fig. 10a) towards point 2 in Figure 14b.

⁴The convex hull is computed using the Qhull library from qhull.org .

5 FINDING NEW DESIGNS

The reduced 2 dimensional domain of the O_{R_r} subspace can be written in set notation as

$$\mathbb{U} = \{\mathbf{u} : \mathbf{u} = \mathbf{U}^T \mathbf{x}, -1 \leq \mathbf{x} \leq 1\}. \quad (16)$$

Here \mathbb{U} is a convex polytope residing in 2 dimensional space, the vertices of which are a subset of the 128 vertices of a 7 dimensional hypercube (χ from Eq. 9) projected onto a 2 dimensional plane. This can be thought of as a silhouette of the 7 dimensional design space on the 2 dimensional subspace. Such projections are called *zonotopes*. Their vertices can be computed using the search algorithm in [34] (or [33]).

The zonotope of the O_{R_r} subspace is plotted as the black line in Figure 14. This represents the limits of the design space, and it is evident that the design space sampled so far (the markers in Fig. 14b) doesn’t encompass these limits. To explore whether improved designs can be found closer to these limits, new designs are generated at the \mathbf{x} ’s labelled 3, 4 and 5 in Figure 15. These \mathbf{u}_R coordinates are selected since they lie in the direction of decreasing O_{R_r} . For completeness, a number of new designs are also generated at points lying within the existing design space. At each point, 5 new designs are randomly generated using the hit and run algorithm, meshes are created, and CFD simulations are run. The five designs at each \mathbf{u}_R coordinate have different \mathbf{x} vectors, but the same \mathbf{u}_R vector. Hence, if the polynomial approximation $O_{Y_p} \approx g(\mathbf{U}^T \mathbf{x}_j)$ is accurate, the five designs at each \mathbf{u}_R vector would be expected to have approximately equal O_{R_r} values. On the other hand, each set of five designs is not guaranteed to have the same u_Y and O_{Y_p} value.

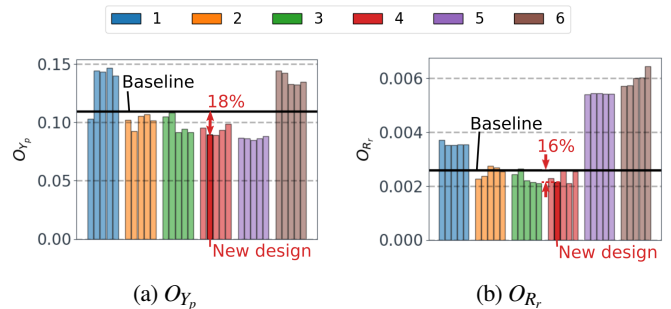


FIGURE 15: Design objectives from CFD evaluations of the new designs. Numbers 1-6 correspond to points 1-6 in Fig. 14.

The resulting values of O_{Y_p} and O_{R_r} for each new design are displayed in Figure 15. It is encouraging that O_{R_r} is similar for the five designs at each point. Lower values of O_{R_r} are attainable by venturing outside of the original sample space, i.e. from point 2 to 3. Moving to the left from point 3 to point 4 moves to a lower O_{Y_p} region, while moving further to point 5 leads to even lower O_{Y_p} at the cost of considerably higher O_{R_r} .

The second design at point 4 is chosen as the new design due to its low values of both design objectives. This design is compared

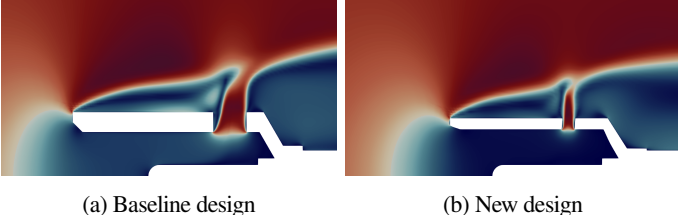


FIGURE 16: Mach number contours of baseline and new designs from CFD at $M=0.8$.

to the baseline in Figure 16. The salient differences are a smaller bleed hole diameter and thinner shroud walls. This achieves an 16% reduction in O_{R_r} , while O_{Y_p} is also 18% lower. For the new probe $O_{R_r}=0.0025$, which would deliver a T_0 uncertainty of $T_0\pm 0.005\%$ for a Mach uncertainty of $M\pm 0.02$.

6 SENSITIVITY TO MANUFACTURING UNCERTAINTY

The objective of Section 5 was to find a new design which can reduce the uncertainty in recovery ratio, R_r , due to an uncertainty in Mach number. An additional concern is the uncertainty in R_r due to manufacturing variations. This can be explored using global sensitivity measures [10] such as Sobol' indices, which can be used to quantify the sensitivity of R_r to each design parameter. However, as will be shown, dimension reducing subspaces can be used to provide additional insights here. To start, a dimension reducing subspace for R_r at $M=0.8$ is constructed:

$$R_r(\mathbf{x}_j) \approx \hat{g}(\hat{\mathbf{U}}^T \mathbf{x}_j) \quad (17)$$

As in Section 4.2, we use variable projection, and select $k=3$ and $m=2$, giving an R^2 score of 0.947. In this case we are concerned with the sensitivity of R_r to perturbations in the design parameters:

$$R_r(\mathbf{x}_j + \Delta) \approx \hat{g}(\hat{\mathbf{U}}^T (\mathbf{x}_j + \Delta)) \quad (18)$$

where Δ represents manufacturing variations injected into each design parameter. The R_r subspace is shown in Figure 17. The arrows demonstrate the influence of perturbing each parameter individually by $\Delta=0.1$. Perturbations are applied to the baseline design, but the decomposition

$$\hat{\mathbf{U}}^T (\mathbf{x}_j + \Delta) = \hat{\mathbf{U}}^T \mathbf{x}_j + \hat{\mathbf{U}}^T \Delta \quad (19)$$

proves that the arrows will be the same anywhere in the R_r subspace. Comparing the magnitude of the arrows indicates what design parameters cause the most significant movement in the R_r subspace

(Hole \emptyset , Kiel \emptyset_{inner} , Kiel \emptyset_{outer} , Hole ellipse, in that order). Additionally, by also considering the contours of R_r , the arrows indicate what parameters are important for a given design. For example, for the baseline design, reductions in the hole diameter are particularly undesirable as they will move the design in a direction perpendicular to the R_r iso-lines.

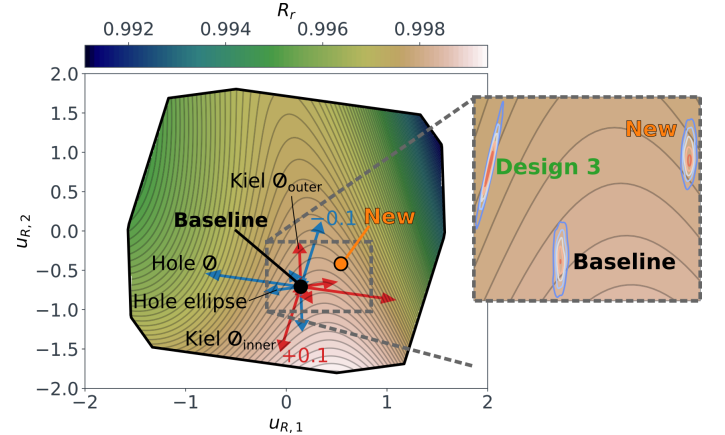


FIGURE 17: Recovery ratio subspace for $M = 0.8$. Arrows demonstrate effect of perturbing each design parameter by ± 0.1 (arrows scaled by 10x). Inset image shows effect of manufacturing uncertainties in selected parameters (Refer to text).

To quantify the uncertainty of R_r due to manufacturing variations, the hole angle, and inner and outer Kiel diameter are replaced by normal distributions $\mathcal{N}(\mu, \sigma^2)$. The original design parameters are set as the mean μ , and $\sigma=0.05\mu$. The σ values chosen all lie within the typical tolerance level for drilling and turning of 0.1mm [35]. For the baseline design and the new design (from Sec. 5), 1000 designs are generated by sampling from the three normal distributions, and kernel density estimates (KDE's) showing the distributions of designs in the subspace are shown in the inset of Figure 17.

The standard deviations of R_r over the KDE distributions in Figure 17 are calculated. For the new design, $\sigma(R_r)=5.1\times 10^{-5}$, which is slightly higher than that of the baseline design, $\sigma(R_r)=3.7\times 10^{-5}$. This indicates that the new design is more sensitive to manufacturing variations in the three design parameters compared to the baseline. The KDE's in Figure 17 show that this is because the new design's distribution lies across more tightly spaced R_r iso-lines. The resulting uncertainty in R_r for the new design is $\pm 1.2\times 10^{-4}$ (at 95% confidence), leading to an uncertainty in temperature of $\pm 0.012\%$. This uncertainty is of a similar magnitude to the T_0 uncertainty due to Mach number uncertainty discussed in Section 2, suggesting it is also important to take manufacturing variability into account. However, moderately large manufacturing tolerances were selected for this example, and they be smaller depending on the manufacturing techniques used.

For a final demonstration of the present approach a third design is shown in the inset within Figure 17. For this design σ is set to be 3 times smaller for the hole and Kiel outer diameters, but 3 times larger

for the Kiel inner diameter. The KDE for this design is therefore stretched out in the direction of the arrows for Kiel \oslash_{outer} . The KDE shows that this direction is almost parallel to the R_r iso-lines. Therefore, the R_r uncertainty for this design is actually relatively low ($(\sigma(R_r) = 2.2 \times 10^{-5})$), despite the large uncertainty in Kiel outer diameter.

7 CONCLUSIONS

This paper has demonstrated how dimension reducing subspaces can be utilised to explore the design space of a temperature probe. The probe's pressure loss coefficient, recovery ratio sensitivity to Mach number, and the recovery ratio itself were found to admit low dimensional structure. Exploration of the subspaces provides a number of important insights:

- The pressure loss subspace is dominated by the Kiel outer diameter, with the bleed hole diameter and angle being of secondary importance. The outer diameter is found to influence the *bluff body*' loss, while the bleed hole diameter and angle affect the behaviour of the jet exiting the bleed holes.
- For the probe considered there is shown to be an optimum vent-to-inlet area ratio that minimises the sensitivity of recovery ratio to Mach number, which can be further reduced with subtle changes to the Kiel outer and inner diameters, and the bleed hole angle.
- By mapping the loss coefficient onto the recovery ratio sensitivity subspace, the trade-off between the two objectives was visualised. This approach highlights regions of the design space that are yet to be explored, and it is used to suggest new designs. Modest reductions of 15% in the loss, and 18% in recovery ratio sensitivity, are achieved over the baseline design. However, the subspaces also provide confidence that the baseline design is already relatively good.
- A dimension reducing subspace for the recovery ratio itself was used to understand the uncertainties due to manufacturing variability. These were shown to be of a similar magnitude to the R_r uncertainty due to Mach number uncertainty. Compared to global sensitivity measures, subspaces provide additional information on what manufacturing tolerances are important for a specific design. Or, it enables the selection of designs which are insensitive to certain design parameters, which may be useful if a particular feature is challenging to manufacture.

This study has demonstrated the potential for using dimension reducing subspaces to design more accurate and less intrusive temperature probes. Important future work could include reducing the recovery ratio's sensitivity to other freestream features, such as turbulence intensity and flow angle. The approach could also be extended to consider radiative errors, more representative conductive errors, the probe's temporal response, and more complex designs such as dual shrouded probes. Dimension reducing subspaces have been used for design space exploration in this paper, but recent

work [36] has demonstrated how they can also be used for design optimisation in future probe design tasks.

ACKNOWLEDGMENT

This work was supported by the Lloyd's Register Foundation-Alan Turing Institute Strategic Priorities Fund (EPSRC grant: EP/T001569/1) and an EPSRC/Rolls-Royce ICASE Award (EPSRC grant: EP/N509103/1). Special thanks go to Prof Paul Tucker from Cambridge University for his guidance. Many thanks also to Samuel Ebenezer and Dr Peter Eiseman from Program Development Company LLC for their help with regards to multi-block structured meshing.

NOMENCLATURE

Abbreviations

<i>CFD</i>	Computational Fluid Dynamics
<i>DOE</i>	Design of Experiments
<i>KDE</i>	Kernel Density Estimate
<i>LHS</i>	Latin Hypercube Sampling
<i>PDF</i>	Probability Density Function
<i>RANS</i>	Reynolds-Averaged Navier-Stokes
<i>SFC</i>	Specific Fuel Consumption

Symbols

η_c	Compressor efficiency
T_0	Stagnation temperature
T_m	Measured temperature
P_0	Stagnation pressure
γ	Ratio of specific heats
Y_p	Stagnation pressure loss coefficient
R_r	Recovery ratio
M	Mach number
O_{Y_p}	Loss design objective
O_{R_r}	Recovery ratio design objective
\mathbf{x}	Full space (7D) coordinates
$\mathbf{x}^L, \mathbf{x}^U$	Lower and upper extents of the design space
k	Maximum order of polynomial
m	Number of reduced dimensions
\mathbf{u}	Dimension reducing subspace coordinates
χ	Parameter space of \mathbf{x}
f, g, h, \hat{g}	Polynomial approximations
\mathbf{U}	Orthogonal matrix
σ	Standard deviation
R^2	Coefficient of determination
\dot{S}_v, \dot{S}_{ht}	Viscous and heat transfer entropy generation rate
Δ	Manufacturing variability in design parameter
\oslash	Diameter

REFERENCES

- [1] Saravanamuttoo, H., 1990. Recommended practices for measurement of gas path pressures and temperatures for performance assessment of aircraft turbine engines. Tech. rep., AGARD report.
- [2] Ubald, B. N., Tucker, P. G., et al., 2018. “Numerical Analysis of an Instrumented Turbine Blade Cascade”. *J. Turbomach.*, **141**(5), pp. 1–12.
- [3] Bonham, C., Thorpe, S. J., et al., 2017. “Combination probes for stagnation pressure and temperature measurements in gas turbine engines”. *Meas. Sci. Technol.*, **29**(1), p. 015002.
- [4] Seshadri, P., Duncan, A., et al., 2019. “Spatial flow-field approximation using few thermodynamic measurements part ii: Uncertainty assessments”. *arXiv preprint arXiv:1908.02934*.
- [5] Kiel, G., 1935. Total-head Meter with Small Sensitivity to Yaw. Tech. rep., NACA Technical Memorandum 775.
- [6] Luo, J., 2009. “Analysis of 3D numerical simulation for an airfoil probe in a compressor”. In 2009 Int. Conf. Comput. Electr. Eng. ICCEE 2009.
- [7] Ng, H. C., and Coull, J. D., 2017. “Parasitic loss due to leading edge instrumentation on a low pressure turbine blade”. *J. Turbomach.*, **139**(4), pp. 1–14.
- [8] Morris, M. D., 1991. “Factorial sampling plans for preliminary computational experiments”. *Technometrics*, **33**(2), pp. 161–174.
- [9] Kucherenko, S., et al., 2009. “Derivative based global sensitivity measures and their link with global sensitivity indices”. *Math. Comput. Simulat.*, **79**(10), pp. 3009–3017.
- [10] Sobol, I. M., 2001. “Global sensitivity indices for nonlinear mathematical models and their monte carlo estimates”. *Math. Comput. Simulat.*, **55**(1-3), pp. 271–280.
- [11] Pinkus, A., 2015. *Ridge functions*, Vol. 205. Cambridge University Press.
- [12] Constantine, P. G., 2015. *Active subspaces: Emerging ideas for dimension reduction in parameter studies*, Vol. 2. SIAM.
- [13] Bahamonde, S., Pini, M., et al., 2017. “Active subspaces for the optimal meanline design of unconventional turbomachinery”. *Appl. Therm. Eng.*, **127**, pp. 1108–1118.
- [14] Seshadri, P., Yuchi, S., et al., 2019. “Supporting multi-point fan design with dimension reduction”. *arXiv preprint arXiv:1910.09030*.
- [15] Seshadri, P., Shahpar, S., et al., 2018. “Turbomachinery active subspace performance maps”. *J. Turbomach.*, **140**(4), p. 041003.
- [16] Beck, J. A., Brown, J. M., et al., 2019. “Active subspace development of integrally bladed disk dynamic properties due to manufacturing variations”. *J. Eng. Gas Turb. Power*, **141**(2), p. 021001.
- [17] Markowski, S. J., and Moffatt, E. M., 1948. “Instrumentation for development of aircraft powerplant components involving fluid flow”. In SAE Tech. Pap.
- [18] Smout, P., 1996. “Probe installation and design criteria”. In VKI Lect. Ser.
- [19] Bonham, C., Brend, M., et al., 2018. “Impact of flow unsteadiness on steady-state gas-path stagnation temperature measurements”. *J. Eng. Gas Turb. Power*, **140**(12).
- [20] Bonham, C., Thorpe, S. J., et al., 2014. “Stagnation temperature measurement using thin-film platinum resistance sensors”. *Meas. Sci. Technol.*, **25**(1).
- [21] Ubald, B. N., 2019. “Multi-fidelity study of complex multi-scale flows concerning temperature probes”. PhD thesis, University of Cambridge.
- [22] de Boer, A., van der Schoot, M., and Bijl, H., 2007. “Mesh deformation based on radial basis function interpolation”. *Comput. Struct.*, **85**, jun, pp. 784–795.
- [23] Schneider, A. J., 2015. “Computational Modeling of Total Temperature Probes”. PhD thesis, Virginia Polytechnic Institute and State University.
- [24] Quickel, R. A., 2019. “Mount Interference and Flow Angle Impacts on Unshielded Total Temperature Probes”. PhD thesis, Virginia Polytechnic Institute and State University.
- [25] Ubald, B. N., Tucker, P. G., and Shahpar, S., 2017. “Assessment of RANS modelling for a complex stagnation probe case”. *AIAA SciTech Forum - 55th AIAA Aerosp. Sci. Meet.*, pp. 1–19.
- [26] Seshadri, P., Yuchi, S., and Parks, G. T., 2018. “Dimension reduction via gaussian ridge functions”. *arXiv preprint arXiv:1802.00515; accepted SIAM-ASA J. Uncertain.*
- [27] Hokanson, J. M., and Constantine, P. G., 2018. “Data-driven polynomial ridge approximation using variable projection”. *SIAM J. Sci. Comput.*, **40**(3), pp. A1566–A1589.
- [28] Golub, G. H., and Pereyra, V., 1973. “The differentiation of pseudo-inverses and nonlinear least squares problems whose variables separate”. *SIAM J. Numer. Anal.*, **10**(2), pp. 413–432.
- [29] Seshadri, P., and Parks, G., 2017. “Effective-quadratures (eq): Polynomials for computational engineering studies”. *J. Open Source Softw.*, **2**, pp. 166–166.
- [30] Denton, J. D., 1993. “The 1993 IGTI Scholar Lecture: Loss Mechanisms in Turbomachines”. *J. Turbomach.*, **115**(4), oct, p. 621.
- [31] Haven, B. A., and Kurosaka, M., 1997. “Kidney and anti-kidney vortices in crossflow jets”. *J. Fluid Mech.*
- [32] Constantine, P., Howard, R., et al., 2016. “Python Active-subspaces Utility Library”. *J. Open Source Softw.*, **1**(5), p. 79.
- [33] Seshadri, P., and Parks, G., 2017. “Effective-Quadratures (EQ): Polynomials for Computational Engineering Studies”. *J. Open Source Softw.*, **2**(11), p. 166.
- [34] Fukuda, K., 2004. “From the zonotope construction to the Minkowski addition of convex polytopes”. *J. Symb. Comput.*
- [35] ASME, 1978. “Preferred Metric Limits and Fits”. *ASME Stand. B4.2*.
- [36] Gross, J. C., Seshadri, P., and Parks, G., 2020. “Optimisation with Intrinsic Dimension Reduction: A Ridge Informed Trust-Region Method”. In AIAA Scitech Forum, pp. 1–21.